Wave power calculations for a wave energy conversion device connected to a drogue

Jerica D. Nolte[a] and R. C. Ertekin[b]
Department of Ocean and Resources Engineering, University of Hawai'i at Mānoa, 2540 Dole St., Holmes Hall 402, Honolulu, Hawaii 96822, USA

(Received 31 May 2013; accepted 6 January 2014; published online 27 January 2014)

We present the numerical modeling of a heaving, point-source wave energy conversion (WEC) device, previously tested by the University of Hawaii at Manoa. The WEC device converts the vertical heave displacements into a rotational motion to generate electrical power; the heave displacements converted are from the WEC system rising with the incoming waves relative to an anchoring system. Two anchoring methods of the WEC device are referred to as the single-body case (moored system) and double-body case (drogue anchored system). The numerical model performs hydrodynamic analysis in the time domain in irregular seas for the single-body or double-body case. We then compare the predictions with the available in-ocean experiments. The computer program written for this purpose solves for the individual body motion and predicts the WEC device's power production over the time series. Moreover, we present the results of the study that shows the effect of the device-damping characteristics and the size and the depth of operation of the drogue on wave-power predictions. © *2014 AIP Publishing LLC*. [http://dx.doi.org/10.1063/1.4862785]

I. INTRODUCTION

Yoshio Masuda's experiments in the 1940s spurred the modern pursuit of wave energy conversion (WEC). He used hundreds of WEC devices to power navigation lights at sea.[1] Many government and private organizations all over the world expanded this idea and have been using buoys to observe earthquakes, tsunamis, and weather conditions. In September 2005, for example, a global net of 1250 drifting buoys was completed, with some 300 new drifters released each year to replace the depleted units.[2] Modern Surface Velocity Program drifters can have batteries in 4–5 packs, each with 7–9 alkaline D-cells, and a transmitter. Depending on the buoy's mission, it could contain other equipment to record air and water temperature, wind speed and direction, salinity, and ocean color. NASA[2] estimates that a drifter transmits an average of 400 days before the batteries are depleted.

Symonds *et al.*[3] pointed out that the acoustic sensors draw between 100 and 200 W of continuous power, which greatly limits the battery life of the buoy to 12–24 hours. Recharging a drained sensor battery is so unreasonable and expensive that many buoys are intended to sink to the bottom after their brief period of operation. Sending batteries and electrical equipment to the bottom of the ocean has a large environmental impact and creates a strong incentive for a freely floating WEC buoy that would be able to charge the batteries.[4] A drogue (or as it is sometimes called, sea anchor) would provide the necessary stable anchor point to a WEC device, relative to the wave motion. This way, wave energy can be converted by a freely floating buoy in very deep waters, where mooring is not economically or technically feasible. A freely floating WEC device would allow the monitoring buoy a longer design life, lessen the environmental impact, and save the operators the cost of replacement buoys.

[a]Present address: Marine Innovation and Technology, 2321 4th Street, Suite 201, Berkeley, California 94710, USA.
[b]Author to whom correspondence should be addressed. Electronic mail: ertekin@hawaii.edu.

The numerical model that has been developed in MATLAB during the course of this research solves the equations of motion in the time domain to also include some of the nonlinearities in the system. From the WEC heave motion, the power is predicted for the system. Solving for the motions of a WEC device in waves has been studied extensively in the frequency domain, e.g., Beatty *et al.*;[5] however, solving the problem in the time domain allows for the inclusion of nonlinearities, and, thus, for a more accurate comparison between the theoretical and experimental data. Count and Jefferys,[6] Falcão,[7] Vicente *et al.*,[8] and Guanche *et al.*,[9] used the theory established by Cummins[10] and Ogilvie,[11] and considered in their research buoy motions in the time domain with the inclusion of linear power take-off (PTO) devices.

Count and Jefferys[6] used linear hydrodynamic theory and experiments to show that the PTO device is the major factor in determining the energy production. Falcão[7] studied an oscillating-body converter with a high-pressure hydraulic PTO that provides a natural way of latching to increase power production in the PTO, among a number of other control methods to optimize power, see, for example, Korde and Ertekin.[12,13] Guanche *et al.*[9] studied a submerged wave energy point absorber, Torres Wave Energy Device that is composed of a floating buoy, a linear generator and hydraulic brakes in regular and irregular waves. Vicente *et al.*[8] numerically modeled a WEC system consisting of a hemispherical buoy in regular and irregular waves.

Vachon[14,15] and Holler[16] experimentally determined the vertical and horizontal drag coefficients for multiple conical drogues. The vertical drag coefficients they found for the conical drogue determine the maximum vertical drag force each drogue can produce. Montgomery and Stroup[17] concluded that a drogue can be scaled to achieve stability where the drogue's motion does not deviate from the direction of the connecting line's tension.

The theory and the numerical model are first presented, followed by the discussion of the results and comparisons with the experimental data obtained earlier by Nolte *et al.*[18] For the case of a freely floating WEC system attached to a drogue, we also have studied different types of buoy and drogue combinations to determine the power output in irregular seas.

II. THEORY

A. Assumptions and coordinate system

The WEC system (Body A) and drogue (Body B) are considered rigid and only act in one degree-of-freedom (heave) due to the external wave force. Therefore, the double-body case will experience two degrees of freedom, one for each body, see Fig. 1. The two bodies are assumed to be far enough apart to not hydrodynamically interact, so the only interaction between the two bodies is through the cable that connects them. The bodies are axisymmetric and are not affected by waves incident from different directions; therefore, the coordinate systems will always align with the direction of the incoming wave propagation. It is noted that the drogue material in practice is a soft tarp-like material but we assume here that it does not collapse, i.e., that it is under tension, as in the experiments of Nolte *et al.*,[18] where a weight is placed below the drogue to prevent it from collapsing. Therefore, the assumption of a rigid body should be acceptable when it comes to providing anchoring to the WEC device and for the purposes of hydrodynamic calculations.

For the calculation of fluid loads, it is assumed that the fluid is inviscid and incompressible and the flow is irrotational. However, in the equations of motion, the drag force on the drogue is included, and it is based on an experimentally determined drag coefficient.

Two right-handed coordinate systems are used in this work. Their origins are at the center of gravity of each body, with the x-axis pointing to the right, the y-axis pointing into the paper and the z-axis pointing up vertically. A two body-coordinate systems exist in the double-body case. Body A, the WEC system, is the body that pierces the free surface and its body-coordinate system is represented by superscript A. Body B, the submerged drogue, is represented by superscript B. For the single-body case, the body-coordinate system is the same as Body A. The irregular surface elevation is calculated with respect to the horizontal position of the center of gravity of Body A. All body accelerations, velocities, displacements, and complex

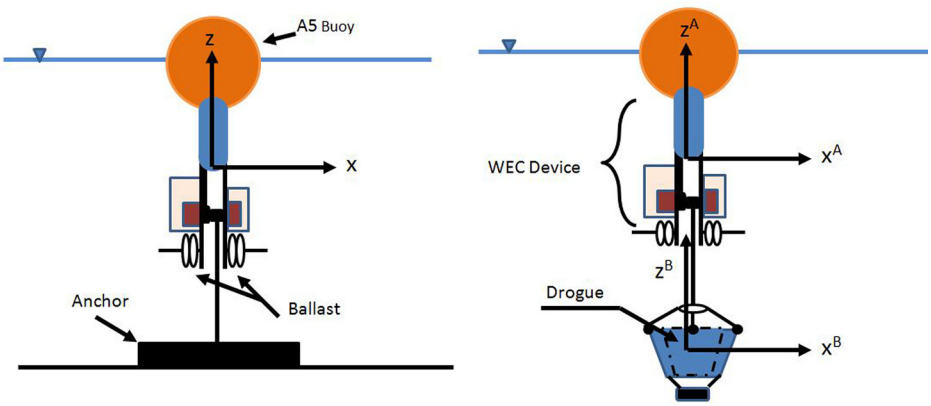

FIG. 1. Coordinate systems used for the single-body case (left) and double-body case (right).

force transfer functions are taken with respect to the origin of each body coordinate system. When we refer to some quantities, such as the force acting on a certain body, we will use the superscript A or B to indicate that the quantity refers to either Body A or Body B.

B. Equations of motion

The equations of motion express the motion of a body in terms of the external forces, mass, damping, and restoring properties. The equations of motion are written by summing all the forces acting on the body, then applying Newton's second law

$$\sum F = m\ddot{z}, \tag{1}$$

where m is the body mass, $\ddot{z}$ is the body acceleration, and $\sum F$ is the sum of all the forces acting on the system. The sum of all the forces that act on a body in this study is given by

$$\sum F = F_m + F_{hs} + W + F_R + F_{PTO} + F_{W_k} + F_{VD}, \tag{2}$$

where

- F_m is the mooring force resulting from the mooring line in the single-body case; or in the double-body case, the force acting on the cable connecting the WEC system and drogue,

$$F_m = -K_m z(t). \tag{3}$$

- F_{hs} is the hydrostatic force resulting from buoyancy. It is composed of two parts, initial (F_{hs_o}) and time-dependent (F_{hs_d}). The initial part is the static buoyancy force acting on the object in the absence of waves and is the constant upward force, Δ, equal to the weight of water displaced. The time-dependent part represents the change in the hydrostatic force as the body moves up and down in waves,

$$F_{hs} = F_{hs_o} - F_{hs_d} = \Delta - \rho g A_w z(t), \tag{4}$$

  where ρ is the mass density of water, g is gravitational acceleration, and A_w is the water-plane area.
- F_{PTO} is the force resulting from the PTO. In this work, the force is caused by a generator and spring. The spring is the constant pull-force spring, which supplies a constant force unrelated to its deflection. The spring is represented by $F_{constant}$. The generator is represented by a viscous dashpot damper, C_{DD}, as power generation dampens the WEC motion. Keller[19] measured the C_{DD} of one of the PTO earlier as 981.14 Ns/m. The C_{DD} is calculated by

$$C_{DD} = \frac{\text{pull force}}{\text{winding velocity}}. \tag{5}$$

In the numerical model, a range of C_{DD} values is evaluated to simulate the effect of different PTOs on the WEC system. The power generation and C_{DD} can only occur when the WEC system has a positive upward velocity or, in the double-body case, has a positive relative velocity, and this, along with other sources of nonlinearity, makes either system nonlinear. It should be noted that C_{DD} will increase or decrease based on the load resistance. The fact that only in part of the wave cycle power is generated can be represented by the Heaviside function $H(\dot{z}(t))$,

$$F_{PTO} = -C_{DD}\dot{z}(t)H(\dot{z}(t)) - F_{constant}, \tag{6}$$

where $\dot{z}$ is the vertical velocity.

- F_R represents the hydrodynamic forces that consist of the added-mass and wave damping forces. The added mass, a, and damping, b, are frequency dependent. The transformation of the forces to the time domain is discussed in Sec. II D. The hydrodynamic force is written as

$$F_R = -a(\sigma)\ddot{z} - b(\sigma)\dot{z}. \tag{7}$$

- F_{W_k} represents the vertical components of the wave exciting forces. The wave exciting forces are the summation of the incoming and diffracting (or scattering) forces, and they are discussed in Sec. II C.
- W represents the body's weight, which is constant, and it is taken as a negative force (as it is in the downward direction),

$$W = -constant. \tag{8}$$

- F_{VD} is the vertical viscous drag force given by

$$F_{VD} = \frac{1}{2}C_D\rho A_p(wv - \dot{z}(t))|(wv - \dot{z}(t))|, \tag{9}$$

where C_D is the vertical drag coefficient, A_p is the projected area, wv is the vertical component of the water particle velocity, and $\dot{z}(t)$ is the vertical velocity of the body. The WEC system or Body A has a shape similar to a circular cylinder, which does not have a large projected area as it moves in heave (small viscous effects). If the viscous drag force of Body A, with $C_D = 0.8$, is included, body motions and power are slightly reduced from the case with no viscous drag on Body A, as we confirmed in this study. The viscous drag for Body B, however, is not negligible, and has a great effect on the results. The C_D used here for the drogue was determined from towing-tank tests conducted by Vachon[15] and Holler[16] who determined that the drag coefficient of a conical drogue is based on the projected area of the drogue, $A_p = \pi(D^2 - d^2)/4$, where D is the top diameter (inlet diameter) and d is the bottom diameter (spill-hole diameter) of the opening of the drogue.

C. Diffraction and Froude-Krylov forces

Three-dimensional mesh models to be used in conjunction with a computer program HYDRAN[20] were created in MATLAB, both for the WEC system and the drogue. These meshes were constructed out of triangular and rectangular panels, see Figs. 2 and 3. The drogue consisted of 572 panels, and the WEC system consisted of 400 panels; the thickness of the drogue was 0.02 m, see Nolte *et al.*[18] and Nolte[21] for other WEC device and drogue dimensions. The number of panels produced converged results for the hydrodynamic and wave exciting forces. The WEC system geometry is not exactly the same as the ocean tested prototype, see Nolte *et al.*[18] The main difference is the bottom of the elliptical cylinder with a major axis

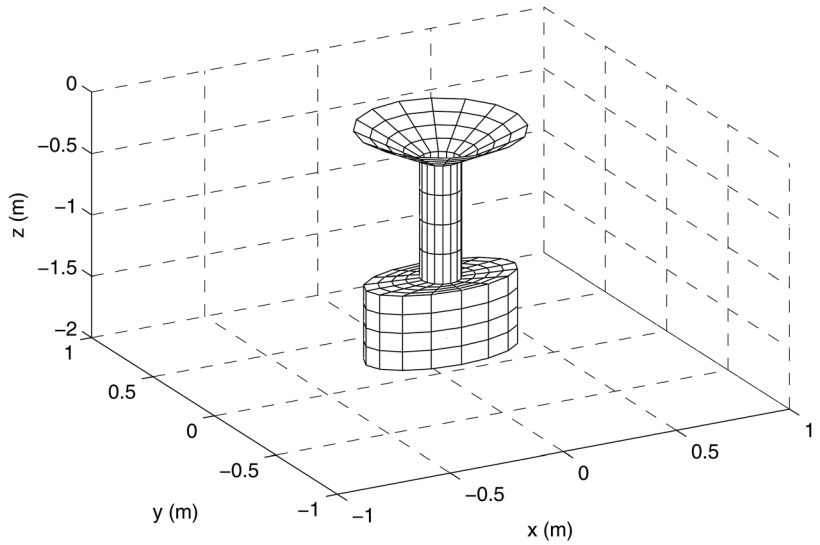

FIG. 2. Three-dimensional mesh of the underwater portion of the WEC system.

of 0.33 m, minor axis of 0.17 m, and height of 0.606 m. To ensure accurate results, the bottom surface area is made equivalent to the bottom surface area of the prototype.

The panel data were entered into HYDRAN[20] that uses the Green-function method to obtain the frequency-dependent, complex transfer functions $H^D(\sigma)$ and $H^{FK}(\sigma)$, where σ is the angular frequency, for the diffraction and Froude-Krylov forces, respectively, and for each body. The summation of these forces results in the wave exciting forces. The details of the theory are briefly discussed in Sec. II G, and the program has been verified through comparisons with other programs and experimental data, see Korde and Ertekin[13] for a list of references.

The diffraction or scattering transfer function is written as

$$H^D(\sigma) = F^D(\sigma)/A(\sigma), \tag{10}$$

where $F^D(\sigma)$ is the complex diffraction force for the angular frequency σ, and $A(\sigma)$ is the corresponding wave amplitude obtained from the irregular sea-surface spectrum.

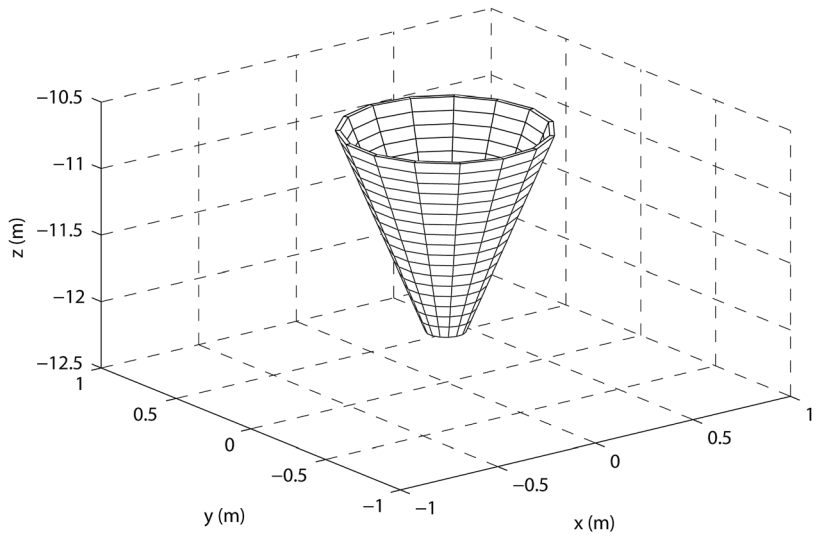

FIG. 3. The drogue is represented by a three-dimensional frustum with a thickness of one panel.

To find the diffraction force in the time domain, the Fourier transform of $F^D(\sigma)$ is taken and the convolution theorem is applied; for details see, e.g., Otto de Kat.[22] It is assumed that the wave motion has been going on for a long time, allowing the transient effects to die out, and the wave process is stationary. Therefore, the time dependent linear diffraction force can be expressed in terms of the transfer function for the regular wave condition,

$$F^D(t) = A(\sigma)H^D(\sigma)e^{i(\sigma t-\epsilon)}. \tag{11}$$

Equation (11) can be rewritten for $H^D(\sigma)$ in terms of its real part, $HR^D(\sigma)$, and its imaginary part, $iHI^D(\sigma)$, and the exponent in terms of the sin and cos functions

$$F^D(t) = A(\sigma)\{HR^D(\sigma) + iHI^D(\sigma)\}\{\cos(\sigma t - \epsilon) + i\sin(\sigma t - \epsilon)\}. \tag{12}$$

Only the real part of Eq. (12) has a physical meaning. The equation for the diffraction force in the time domain can therefore be written as

$$F^D(t) = \sum A(\sigma)(HR^D(\sigma)\cos(\sigma t - \epsilon) - HI^D(\sigma)\sin(\sigma t - \epsilon)), \tag{13}$$

see, e.g., Chitrapu and Ertekin.[23]

The Froude-Krylov forces, due to the incident wave pressure alone, can be obtained by using a similar method. The Froude-Krylov force transfer function is $H^{FK}(\sigma)$, and $A(\sigma)$ is the corresponding wave amplitude found from the irregular sea surface calculations. This gives the complex Froude-Krylov force,

$$F^{FK}(t) = A(\sigma)H^{FK}(\sigma)e^{i(\sigma t-\epsilon)}. \tag{14}$$

The same assumptions and methods to find the diffraction force are made to obtain the real part of the Froude-Krylov force in the time domain,

$$F^{FK}(t) = \sum A(\sigma)(HR^{FK}(\sigma)\cos(\sigma t - \epsilon) - HI^{FK}(\sigma)\sin(\sigma t - \epsilon)). \tag{15}$$

The wave exciting forces are obtained by the summation of the Froude-Krylov and diffraction forces at each time, t.

D. Radiation force

The hydrodynamic forces are calculated in the frequency domain and converted to the time domain by use of the theory of Cummins,[10] who studied the hydrodynamic problem of an ideal fluid in the time-domain, to find a representation for the linear pressure forces; also see Count and Jefferys.[6] Ogilvie[11] proved the relationship between the frequency dependent added mass and damping to the time domain counterparts by using the Fourier transform theory. From these works, the following equation relating the frequency-dependent hydrodynamic coefficients to the time domain coefficients is written:

$$A_{33} = a(\sigma_1) + \frac{1}{\sigma_1}\int_0^\infty K(\tau)\sin(\sigma_1\tau)d\tau, \quad K(\tau) = \frac{2}{\pi}\int_0^\infty b(\sigma)\cos(\sigma\tau)d\sigma, \tag{16}$$

where A_{33} is the genuine added mass or $a(\infty)$, a is the frequency dependent added mass, τ is the time lag, σ_1 is a specific frequency where the frequency dependent added mass is known, $K(\tau)$ is the Kernel or retardation function, and b is the frequency dependent radiation damping as before.

Given Eqs. (16) and (7), it is now possible to solve for the hydrodynamic forces acting on the body due to small arbitrary motions in the time domain. The radiation force on a body is written as

$$F_R = -A_{33}\ddot{z}(t) - \int_0^t K(\tau)\dot{z}(t-\tau)\,d\tau. \tag{17}$$

The first term on the right-hand side of Eq. (17) represents the forces due to the acceleration of the structure. The second term represents the fluid memory effect that incorporates the energy dissipation due to the radiated waves caused by the motion of the structure.

E. Single-body case

The equations of motion in the time domain for the single-body case represent a moored, surface piercing body. The sum of the static external forces can be written as

$$\sum F = F_{hs} - W - F_m. \tag{18}$$

The static internal forces show the WEC's constant pull force spring, $F_{constant}$, is a fraction of the mooring force,

$$F_m = \alpha F_{constant}, \tag{19}$$

where α is the ratio of the two diameters of the spool. The internal dynamic forces are such that $F_{constant}$ and the torque of the WEC's generator are equal to the mooring force, and this is written as

$$F_m = \alpha F_{constant} + C_{DD}\dot{z}(t)H(\dot{z}(t)). \tag{20}$$

By substituting Eqs. (1), (4), and (20) into Eq. (18), adding wave exciting forces and hydrodynamic forces, canceling the weight and static mooring force with the initial hydrostatic force, and adding likewise terms, the equation for the single-body case becomes

$$(m + A_{33})\ddot{z}(t) + \int_0^{\tau_{max}} K(\tau)\dot{z}(t-\tau)d\tau + C_{DD}\dot{z}(t)H(\dot{z}(t) + \rho g A_w z(t) = F_{W_k}. \tag{21}$$

F. Double-body case

The equations of motion for the double-body case represent a freely floating two-body system, connected to each other by a cable, with Body A piercing the free surface and Body B fully submerged and ballasted. The double-body case has two equations of motion, one for each body. Body A's equations of motion, was found to be similar to the single-body case, except that the velocity is the relative velocity of the two bodies. The equation of motion for Body A is given by

$$(m^A + A^A_{33})\ddot{z}^A(t) + \int_0^{\tau_{max}} K^A(\tau)\dot{z}^A(t-\tau)d\tau + C_{DD}\dot{z}_{rel}(t)H(\dot{z}_{rel}(t)) + \rho g A^A_w z^A(t) = F^A_{W_k}, \tag{22}$$

where $\dot{z}_{rel} = (\dot{z}^A(t) - \dot{z}^B(t))$ is the relative velocity between Body A and Body B.

Body B is attached to Body A by a cable, and is to remain relatively motionless to act as a floating anchor point for Body A. The drogue should, in principle, allow the WEC system's PTO to work approximately the same as when moored to the sea floor. The sum of static external forces acting on the drogue is

$$\sum F = F^B_{hs} - W^B + F_m. \tag{23}$$

As in the single-body case, Eqs. (1), (4), and (20) can be substituted into Eq. (23) to obtain

$$m^B\ddot{z}^B = F^B_{hs_o} - F^B_{hs_d} - W^B + \alpha F_{constant} + C_{DD}\dot{z}_{rel}(t)H(\dot{z}_{rel}(t)). \tag{24}$$

The external dynamic forces, the radiation, viscous drag, and wave exciting forces, are now added to obtain

$$m^B \ddot{z}^B = F^B_{hs_o} - F^B_{hs_d} - W^B + \alpha F_{constant} + C_{DD}\dot{z}_{rel}(t)H(\dot{z}_{rel}(t)) + F^B_R + F^B_{W_k} + F^B_{VD}. \quad (25)$$

Because Body B is fully submerged, the hydrostatic force, F_{hs_d}, is zero. The drogue is away from the free surface, and, therefore, the hydrodynamic radiation damping is also negligible by assumption; HYDRAN[20] calculations confirmed that the radiation damping for the drogue is indeed negligible.

The equations of motion of Body B are now written as

$$(m^B + A^B_{33})\ddot{z}(t) - F^B_{hs_o} + F^B_{hs_d} + W^B - \alpha F_{constant} - C_{DD}\dot{z}_{rel}(t)H(\dot{z}_{rel}(t)) - F^B_{VD} = F^B_{W_k}. \quad (26)$$

Similar to Body A, Eq. (23) shows that the weight of the drogue is equal to the initial hydrostatic force and the mooring force (see Nolte[21] for the analysis of free-body diagrams for both the single- and double-body cases). However, these forces cannot be canceled as in Body A because of the conditions set on the connecting line:

1. If $z_{rel} < 0$ then the connecting cable is slack and no power can be generated (Body A and Body B act as single bodies). Therefore, $F_m = \alpha F_{constant} + C_{DD}\dot{z}_{rel} = 0$ ($\alpha F_{constant} = 0$ and $C_{DD} = 0$). This occurs when Body B's displacement is greater than Body A.
2. If $z_{rel} > 0$ then the connecting cable is taut. This only means that the static mooring force, $F_m = \alpha F_{constant}$, is acting on the system. This occurs only when Body A has a positive displacement larger than Body B. The displacements are relative to the respective bodies' initial starting positions designated by the initial conditions.
3. If $\dot{z}_{rel} > 0$ and $z_{rel} > 0$ then it is possible for the PTO to capture wave energy (C_{DD} and $\alpha F_{constant}$ forces are acting on the system). $\dot{z}_{rel} > 0$ occurs when Body A's velocity is greater than Body B. The maximum relative velocity is when Body A has a positive velocity and Body B has a negative velocity. This can cause jerks on the line. On the other hand, if $\dot{z}_{rel} < 0$ then $C_{DD} = 0$ and the PTO will not produce power. This arises when Body A's velocity is less than Body B's velocity.

To remove improbable data, a tolerance was set for $\dot{z}_{rel}$ and z_{rel}, 0.001 m/s and 0.001 m, respectively. Therefore if power was predicted for a relative displacement and velocity smaller than these values, the power is set to zero at that time. This is done after solving for the equations of motion.

G. Review of potential theory

The problem of a body's interaction with waves can be solved by means of linear potential theory and through a series of boundary-value problems as it is done in HYDRAN.[20] Assuming small-amplitude, linear progressive waves and correspondingly small motions of a body with no forward speed, the total velocity potential is the sum of the incident potential, diffraction potential, and radiation potentials. The total velocity potential, ϕ, can be written as

$$\phi = \phi_0 + \phi_7 + \sum_{j=1}^{6} \phi_j, \quad (27)$$

where ϕ_0 is the incident potential, ϕ_7 is the diffraction potential, and ϕ_j is the radiation potential for $j = 1, ..., 6$ degrees of motion. The incident potential represents the potential of the incoming waves with no obstruction present, and in constant water depth. The diffraction potential represents the potential of diffracted waves acting on a body that is fixed. The radiation potential is the potential when the body oscillates within prescribed motions in an otherwise calm fluid.

All potentials $(\phi_0, ..., \phi_7)$ must satisfy Laplace's equation,

$$\nabla^2 \phi_j = 0, \quad \text{in the fluid domain,} \tag{28}$$

and the boundary conditions,

$$\frac{\partial^2 \phi_j}{\partial t^2} + g \frac{\partial \phi_j}{\partial z} = 0, \text{ on the still-water surface,} \tag{29}$$

$$\frac{\partial \phi_0}{\partial n} = -\frac{\partial \phi_7}{\partial n}, \text{ on the fixed body surface,} \tag{30}$$

$$\frac{\partial \phi_j}{\partial n} = n_j, \text{ on the mean body surface for } j = 1, ..., 6, \tag{31}$$

$$\frac{\partial \phi_7}{\partial n} = 0, \text{ on the fixed seafloor,} \tag{32}$$

where n is the unit normal vector directed into the body, z is the vertical coordinate, t is time, and g is the acceleration due to gravity, and n_j, $j = 4, 5, 6$, are the components of the vector product of the position vector and n.

In addition to these conditions, the radiation and diffraction potentials must also satisfy the radiation (or the Sommerfeld) condition,

$$\lim_{R \to \infty} \sqrt{R} \left(\frac{\partial}{\partial R} + ik \right) \phi_j = 0, \tag{33}$$

for $j = 1, ..., 7$, where R is the radial distance from the center of the body on the still-water surface, and k is the wave number as the solution of the linear dispersion relation.

Once all potentials are known through the use of the Green-function method, linearized Euler's integral is used to determine the pressures, and thus, to calculate the Froude-Krylov force, diffraction force, and added-mass and damping coefficients.

III. NUMERICAL MODEL

We developed a MATLAB program that can be used for a single wave spectrum or it can provide continuous output of power given a surface-elevation time series that is a result of significant wave height, H_s, and peak wave period, T_p, pairs obtained from monthly or seasonally observed wave data. The computational procedure of the numerical model can be outlined as seen in the flow chart of Fig. 4.

The inputs are given in the top row of the chart. The spectrum is used to create a time series of the irregular sea-surface elevation. The wave exciting force transfer functions and the sea-surface elevation are used to generate the time series of the wave exciting forces. Also, the given added-mass and damping coefficients are transformed into the time domain. The time domain added-mass and damping coefficients, time series of wave exciting forces, body characteristics (weight and dimensions), and PTO characteristics are then used to solve for the equations of motion to determine the vertical component of the body velocity and displacement. The body velocity and PTO characteristics are finally used to generate the time series of the power output.

A. Solving the equations of motion

Filon's method is used to solve for the radiation Kernels from the frequency-dependent damping coefficients,

$$K(\tau) = \int_0^{\sigma_f} b(\sigma) \cos(\sigma \tau) d\sigma, \tag{34}$$

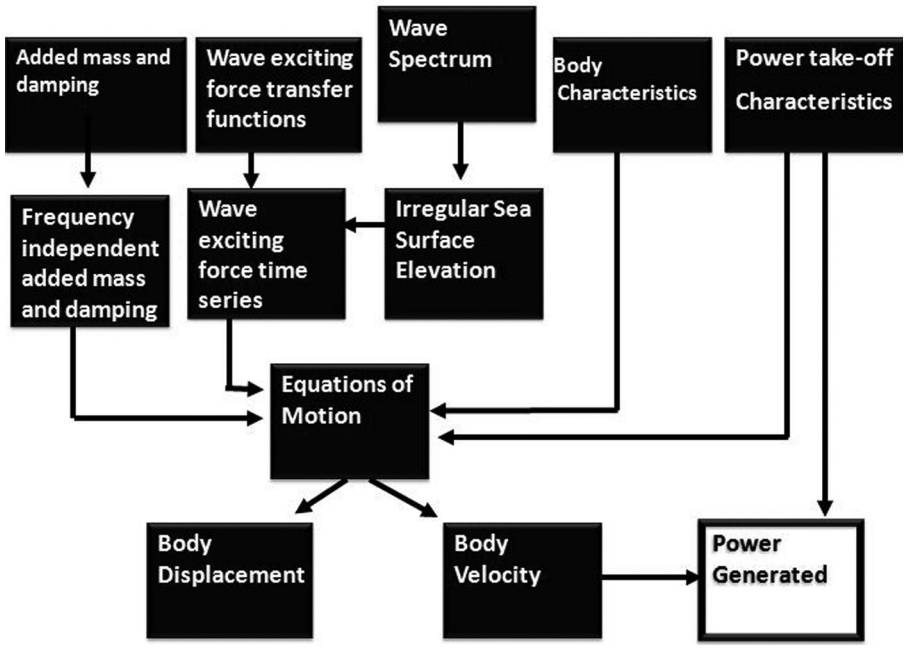

FIG. 4. Program flow chart.

where σ_f is the max frequency where $b(\sigma)$ becomes zero, e.g., Otto de Kat.[24] The basic methodology of Filon's method is that the function $f(x)$ is smooth over the interval (a,b) and can be approximated by a polynomial so that the integration over the sub-intervals is performed analytically. The entire integration can be approximated by the summation of discrete integrals over the sub-intervals. Full details of Filon's method are given by, e.g., Otto de Kat.[22]

Once the frequency-independent added mass and kernel functions are calculated by HYDRAN, the memory effect integrals in Eqs. (21) and (22) are evaluated. The memory effect integral for the single-body case is written as

$$M(t) = \int_0^\infty K(\tau)\dot{z}(t-\tau)d\tau, \tag{35}$$

where $K(\tau)$ is the Kernel function and $\dot{z}$ is the velocity of the center of gravity of the body. The upper limit of the memory effect integral can be replaced by τ_{max}, which is the time when $K(\tau)$ reaches a constant value. In this study, a value of 30 s is selected for τ_{max}. The time interval of $\Delta\tau$ was chosen the same as the interval of the time integration, Δt. This allows the time history of velocity and the Kernel functions to be specified at the same time intervals. A value of $\Delta t = \Delta\tau = 0.2$ s has been chosen in this study. A trapezoidal integration scheme is used to evaluate the memory intervals. It should be noted, that when $t \leq \tau$, velocity is equal to zero.

1. Rewriting the equations of motion

To solve the equations of motion, Eqs. (21), (22), and (26) are first rewritten in the form of a 1st-order ordinary differential equation (ODE) such as

$$\frac{dv}{dt} = f(t, v).$$

The 1st-order ODE is solved if the initial conditions for all the variables are known using the 4th-order Runge Kutta method. The right-hand side of Eq. (36) below is evaluated four times at each time step to find the extrapolation of the solution at the next time step. The equations of

motion for the bodies in this work contain unknowns and also the derivatives of the unknowns on the right-hand side of the equation.

The equations of motion need to be rewritten such that the right-hand side does not include the accelerations. The forces that do not depend on accelerations can be grouped into the term F_0. The general procedure is the same for all of the bodies, so only the single-body case is described here. All terms of the single-body equation, Eq. (21), not dependent on acceleration are grouped into F_0, see the following equation:

$$F_0 = -\int_0^{\tau_{max}} K(t-\tau)\dot{z}(\tau)d\tau - C_{DD}\dot{z}(t)H(\dot{z}(t)) - F_{hs_d}z(t) + F_{W_k}. \tag{36}$$

Equation (36) can be substituted into Eq. (21), which can now be written as

$$(m + A_{33})\ddot{z}(t) = F_0. \tag{37}$$

Dividing by the total mass, Eq. (37) becomes

$$\ddot{z}(t) = F_0(m + A_{33})^{-1}, \tag{38}$$

or it can be written as two coupled ODEs, one for the position, z, and one for the velocity, $\dot{z}(t)$

$$\frac{d\dot{z}(t)}{dt} = f(\dot{z}(t), z(t), t), \qquad \frac{dz(t)}{dt} = \dot{z}(t). \tag{39}$$

2. Time integration

The method used here for time integration is also used by Chitrapu and Ertekin[23] to obtain the six degrees-of-freedom motions of a single body. The difference here is that we do have two bodies in one case for which four 1st-order ODEs are needed (two for each body). The initial velocities and displacements of all bodies are set to zero. For the single-body case, the 4th-order Runge Kutta method can be written as

$$\begin{aligned}
s(t,1) &= \Delta t f(t, \dot{z}(t), z(t)),\\
d(t,1) &= \Delta t f(t, \dot{z}(t)),\\
s(t,2) &= \Delta t f\left(t + \frac{\Delta t}{2}, \dot{z}(t) + \frac{s(t,1)}{2}, z(t) + \frac{d(t,1)}{2}\right),\\
d(t,2) &= \Delta t f\left(t + \frac{\Delta t}{2}, \dot{z}(t) + \frac{s(t,1)}{2}\right),\\
s(t,3) &= \Delta t f\left(t + \frac{\Delta t}{2}, \dot{z}(t) + \frac{s(t,2)}{2}, z(t) + \frac{d(t,2)}{2}\right),\\
d(t,3) &= \Delta t f\left(t + \frac{\Delta t}{2}, \dot{z}(t) + \frac{s(t,2)}{2}\right),\\
s(t,4) &= \Delta t f(t + \Delta t, \dot{z}(t) + s(t,3), z(t) + d(t,3)),\\
d(t,4) &= \Delta t f(t + \Delta t, \dot{z}(t) + s(t,3)),
\end{aligned} \tag{40}$$

$$\begin{aligned}
\dot{z}(t + \Delta t) &= \dot{z}(t) + \frac{1}{6}[s(t,1) + 2s(t,2) + 2s(t,3) + s(4)],\\
z(t + \Delta t) &= z(t) + \frac{1}{6}[d(t,1) + 2d(t,2) + 2d(t,3) + d(4)].
\end{aligned} \tag{41}$$

The right-hand side of Eq. (39) is evaluated four times at each step as shown in Eq. (40). The initial forces are determined from the user defined body's initial conditions. The initial forces are then summed to obtain the total force acting on the body. Thus, F_0, m, and A_{33} are

known from the body's initial conditions. This solves the right-hand side of Eq. (38), which is used to evaluate s(1) and d(1) in Eq. (40). The body's motion is updated with the value of s(1) and d(1) and the forces are computed again with the updated values to calculate s(2) and d(2). This is repeated to get s(3), s(4), d(3), and d(4). The body's motions for the next time step are obtained with Eq. (41). Note that the memory effect integrals in Eq. (35) are evaluated by the trapezoidal method four times at each time step (once for s(1),…,s(4)).

In the double-body case, the bodies are coupled, or the motion of Body A depends on the motion of Body B, and vice versa. Therefore, the equations of motion for both bodies are solved simultaneously for each body's velocity and displacement. The 4th-order Runge Kutta method of solution is similar to the single-body case, except that conditions are set at each half step to determine if the connecting line is slack or taut and if the PTO is generating power (the conditions are listed in Sec. II F).

Because of the high-order of the 4th-order Runge Kutta method used to solve the equations of motion, the process is somewhat similar to doing iteration. Through the 4th-order Runge Kutta method, the body velocities are solved four times for each time, t. This, along with a small Δt, should only contain a small error in the body velocities and displacements found.

IV. POWER PERFORMANCE

The time series of the power output for the single-body and double-body cases, respectively, are

$$P(t) = C_{DD}(\dot{z}(t))^2\beta\,, \quad P(t) = C_{DD}(\dot{z}_{rel}(t))^2\beta, \tag{42}$$

where $P(t)$ is the time series of the power output and β is the gearing ratio. The gearing ratio is necessary to correlate the velocity of the body to the velocity the generator is rotating at and it is an empirical quantity. In this work, $\beta = 13$ is built into the system. Larger gearing ratios are not desirable as they would cause larger friction and thus difficulty in the turning of the gears; smaller gearing ratios would tend to lower the power output.

V. RESULTS AND DISCUSSION

For both the single- and double-body cases, the Bretschneider spectrum is used for the significant wave height, $H_s = 0.28\,\text{m}$, peak period, $T_p = 15.5\,\text{s}$, $d\sigma = 0.01\,\text{rad/s}$, $\alpha F_{constant} = 181\text{N}$ and $C_{DD} = 981\,\text{Ns/m}$, for frequencies that range from $0.2\,\text{rad/s}$ to $2\,\text{rad/s}$ (to compare with the experimental data of Nolte *et al.*[18]). Also, the motions and power output were calculated for a range of C_{DD} values to assess the effect of C_{DD} on the results as we discuss later.

Clearly, $d\sigma$ should be sufficiently small to accurately represent the random seas with the correct variance and peak period. When going from a spectrum to time-dependent surface elevation, the phase information is provided by a random number generator. The surface elevation is used to solve both cases for all values of C_{DD}. It is important to emphasize that the maximum value and location of the motions and power peaks will change with a different selection of random phase angles used to create the random time series data. The root mean square (RMS), however, should remain the same for different time series obtained by different set of (random) phase angles.

A. Single-body case

The infinite-frequency added mass for the single-body case, Body A, is taken as 78 kg. The Kernel function, seen in Fig. 5, shows that $K(\tau)$, reaches near a constant value with Filon's method at approximately $\tau = 30\,\text{s}$, and vanishes.

Figure 6 shows the WEC system's heave displacement compared with the surface elevation. This shows that the WEC system closely follows the waves with slightly smaller amplitudes. This is similar to what is observed in the experimental trials, see Nolte *et al.*[18]

The resulting spectra are shown in Fig. 7. The spectra show a difference in amplitudes at $\sigma = 0.4\,\text{rad/s}$ to $0.5\,\text{rad/s}$, where most of the energy is being extracted from the waves. Similar

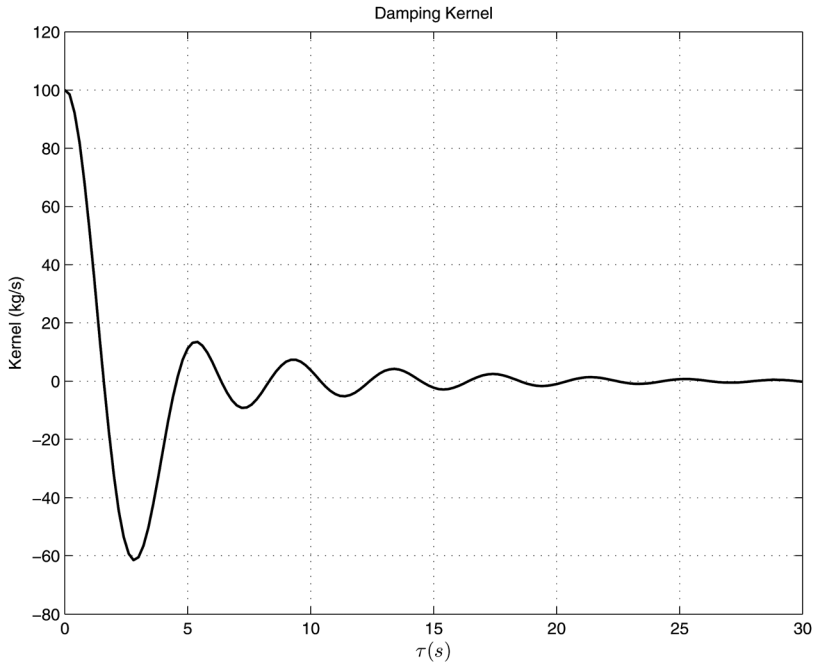

FIG. 5. Kernel of the WEC system, Eq. (34).

to the experimental data, the significant heave double-amplitude is $Z_s = 0.2752\,\text{m}$ and the significant wave height is $H_s = 0.28\,\text{m}$. For this particular sea-surface elevation, the results closely resemble a linear system. However, because the system is nonlinear due to the presence of the drag force and the fact that the system generates power only in one half of the wave cycle, the response amplitude operator (RAO) (found to be about 1.0) is only applicable to this spectrum. If the RAO is desired for another spectrum, the time series has to be recalculated and another RAO must be obtained. The resulting time series of power output is shown in Fig. 8. The

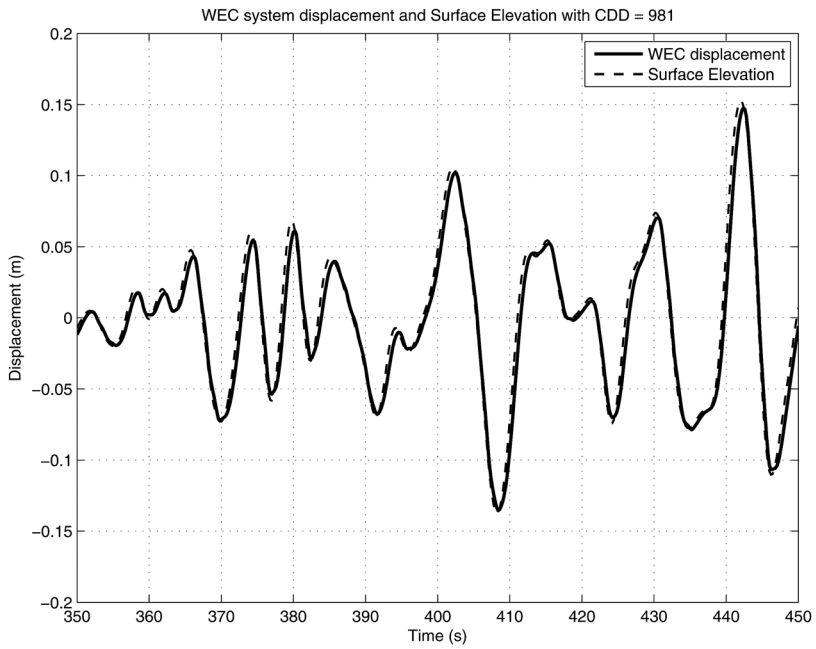

FIG. 6. Overlay of the WEC system heave displacement versus surface elevation.

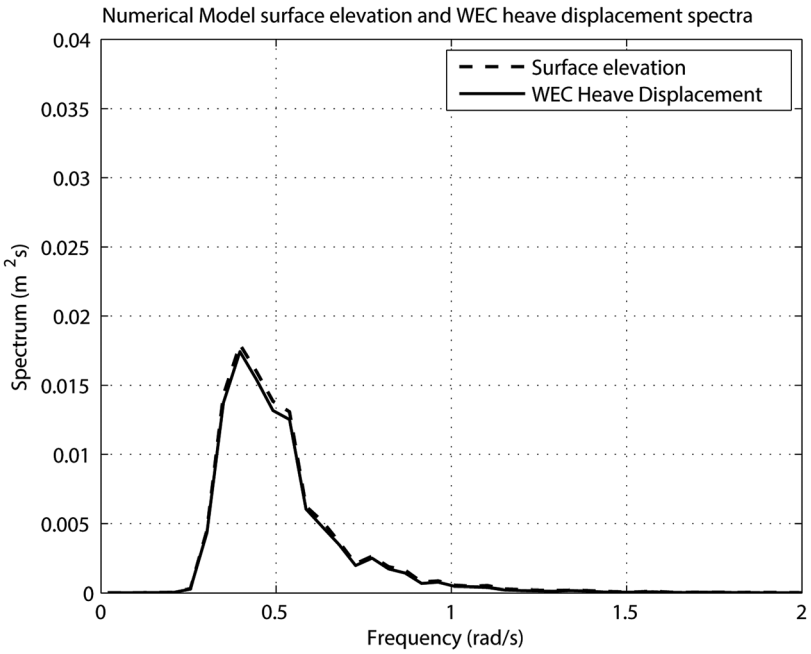

FIG. 7. Comparison of the WEC system heave displacement and surface elevation spectra.

maximum power output is around 140 W. This is just under double of the maximum peak observed in the ocean experiments, and is a result of the random phases that could produce this spike. The maximum peak power output and the average peak output over the time series are shown by the top and bottom horizontal lines, respectively, in Fig. 8. The average peak power output over the time series is 13.9 W, which is higher than the experimental power output (10.2 W), seen in Table I.

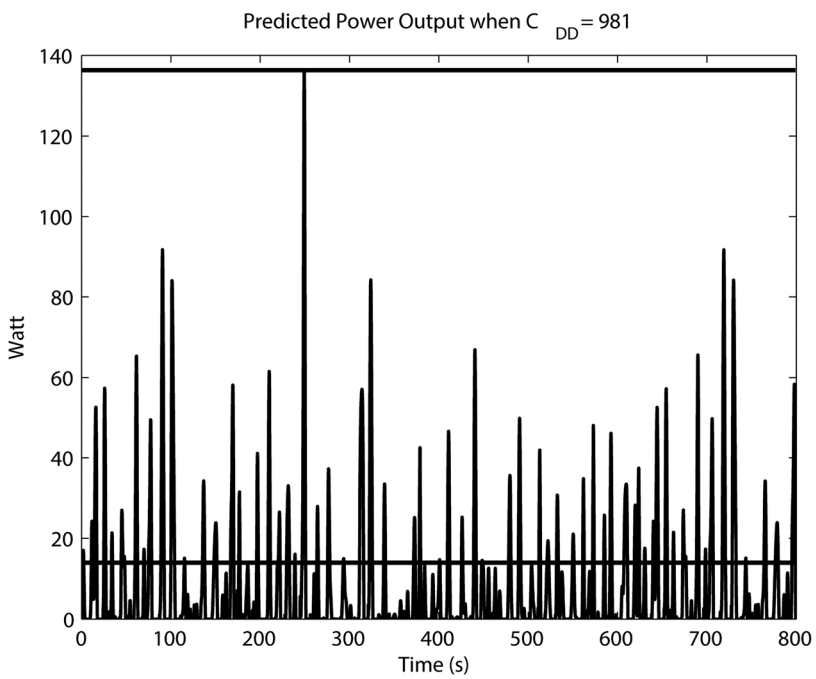

FIG. 8. Time series of single-body power output. The top line is the maximum power predicted, and the bottom line is the average power predicted.

TABLE I. Comparison between the numerical and experimental results for the single-body case.

Case	Numerical	Experimental
Average of power peaks	13.9 W	10.2 W
Maximum peak power	136.9 W	87 W
Power RMS	16.9 W	6.8 W

To double check the accuracy of the single-body program, C_{DD} was set to zero; therefore, no PTO was acting on the system and the body should act like a small floating cylinder. This linear system resulted in the body riding the wave, with the main variations caused by the memory integral.

1. Different PTOs

We next discuss the effect of C_{DD} on the power output. To do this, we vary C_{DD} from 500 Ns/m to 2500 Ns/m. Fig. 9 shows that $C_{DD} = 2500$ Ns/m is not ideal for the WEC system. The body is overdamped, has mostly negative velocity, and is thus unable to produce power. As C_{DD} decreases, the positive velocity increases. Therefore, for power generation, there exists a trade off between the value of C_{DD} and the velocity. A higher C_{DD} will generate more power, but a too high value of C_{DD} will decrease the positive velocity and thus decrease the power output. Also, the larger the C_{DD} is, the greater the nonlinear effects on the body motion are. A difference is seen in smoothness of the velocity curves. The difference is caused by the C_{DD} restricting the body's motion when the body has positive velocity. For smaller C_{DD} values, the body's motion is very close to the sea-surface elevation and the body behaves like a linear system.

The overdamping with $C_{DD} = 2500$ Ns/m is also seen in Table II, as it has low power output and the smallest RMS. $C_{DD} = 500$ Ns/m creates a system that is underdamped as it produces the least power, with an RMS similar to the case of $C_{DD} = 2000$ Ns/m. From Table II, it seems that an optimum C_{DD} value is near 1500 Ns/m for this case.

B. Double-body case

The relative displacement in this case is shown in Fig. 10. The positive relative displacement is only a few centimeters and has a similar amplitude compared with the experimental data given in Nolte *et al.*[18]

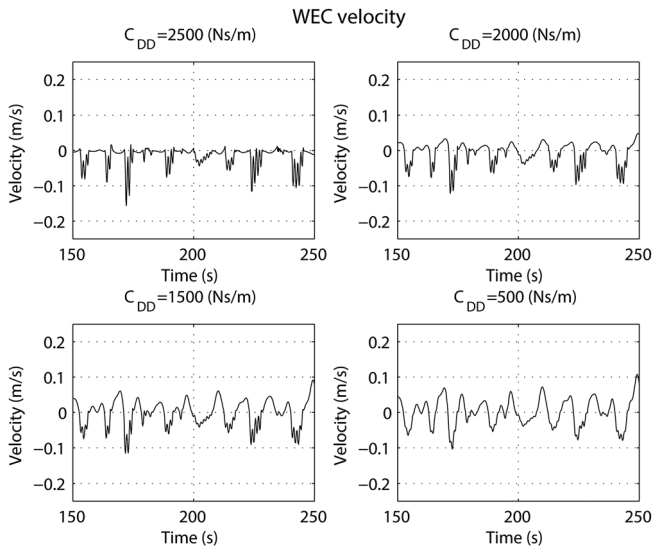

FIG. 9. WEC system velocity for various values of the generator viscous dashpot damper, C_{DD}.

TABLE II. Comparison between different C_{DD} for the single body case.

C_{DD} cases	2500 Ns/m	2000 Ns/m	1500 Ns/m	500 Ns/m
Average of power peaks	0.83 W	7.74 W	18.7 W	8.56 W
Maximum peak power	33.46 W	60.18 W	165 W	75.61 W
Power RMS	1.67 W	8.97 W	22.7 W	10.17 W

The resulting time series of power output is shown in Fig. 11. The maximum peak power output and the average peak output over the time series are shown by the top and bottom horizontal lines in Fig. 11, respectively. The maximum power output in Fig. 11 is around 14 W and average peak output over the time series is 4.04 W, which is slightly higher than the experimental peak power output (2.32 W). Also more peaks are predicted by the numerical model than seen in the experimental data, and this is reflected by the higher RMS, see Table III.

The spectrum of the relative displacement between Body A and Body B is shown with the spectrum of the surface waves in Fig. 12, where the double-body case does not have a peak frequency, but shows a more level response. Slightly more energy is seen at the lower frequencies, when the waves are longer and there is more time for the connecting line to be pulled taut; resulting in Body A having a greater displacement than Body B. The significant double amplitude of the relative displacement of the double-body case is $Z_s = 0.19$ m, which is noticeably lower than the relative displacement of the single-body case. The double-body case cannot harness most of the energy in the surface waves because Body B does not provide a consistent anchor point, unlike the sea floor in the single-body case.

To check the accuracy of the double-body program further, C_{DD} and αF were set to zero, so no PTO was acting on the system. Body A reacted like a floating cylinder and had an RAO of 1.0 (the same as in the single-body case) as expected. Body B sunk, which agreed with the predicted outcome, as Body B is negatively buoyant, and according to the equations of motion with no (PTO), is no longer connected to Body A.

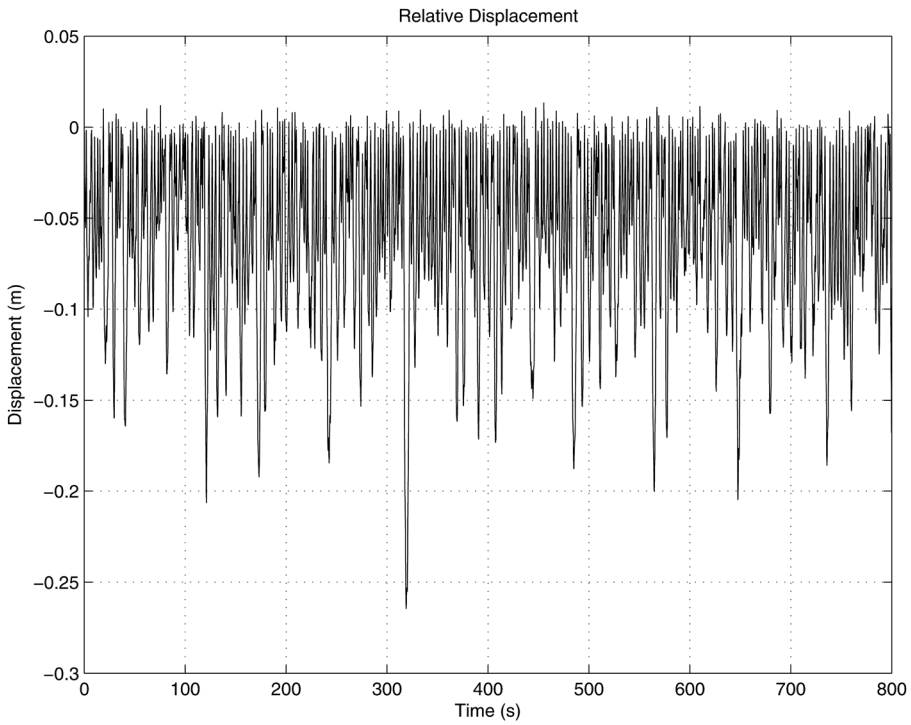

FIG. 10. The relative displacement of the double-body system.

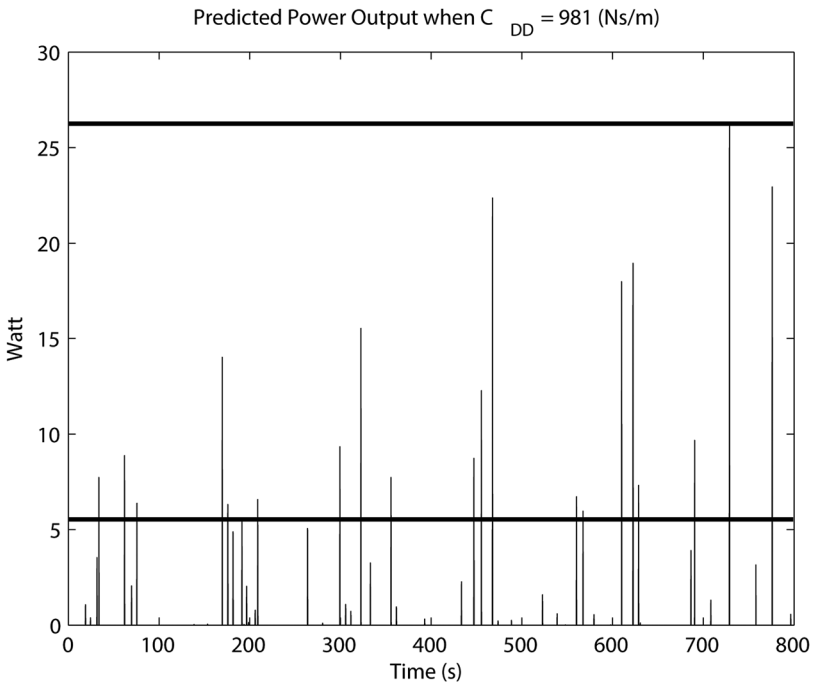

FIG. 11. Time series of double-body power output.

1. Different PTOs

Figure 13 shows that the case with lower C_{DD} experiences more instances of positive relative displacement and smaller negative relative displacement. However, $C_{DD} = 2000\,\mathrm{Ns/m}$ and $1500\,\mathrm{Ns/m}$ have larger positive relative displacements. Also the larger the C_{DD} is, the more nonlinear effects present in the relative displacement. A difference is seen in the smoothness of the data. The differences are caused by the C_{DD} and $\alpha F_{constant}$ restricting the body's motion and pulling Body B up when the system has positive velocity and displacement. For smaller C_{DD} values, the body's motion is very close to the sea surface elevation and the body acts like a linear system.

Similar to the results obtained for the relative displacement, the larger the C_{DD} is, the more nonlinear effects are present in the relative velocity. A difference is seen in the smoothness of the data. The differences are caused by the C_{DD} and $\alpha F_{constant}$ restricting the body's motion and pulling Body B up when the system has positive velocity and displacement.

Figure 14 shows the positive relative displacement, when power generation occurs (relative displacement and relative velocity are positive at the same time). Figure 14 shows that $C_{DD} = 2500\,\mathrm{Ns/m}$ is not ideal for this WEC system as there are no instances where the relative displacement and relative velocity are both positive at the same time. Therefore, the system is overdamped in the double-body case with the drogue. Also Fig. 14 shows that as C_{DD} decreases, the relative displacement during power generation decreases, but the number of instances of positive relative displacement increases. This means that the lower the C_{DD} values are, the more Body B is able to act as a stable anchor point.

TABLE III. Comparison between the numerical and experimental results for the double-body case.

Case	Numerical	Experimental
Average of power peaks	4.04 W	2.32 W
Maximum peak power	14.0 W	4.15 W
Power RMS	0.65 W	0.059 W

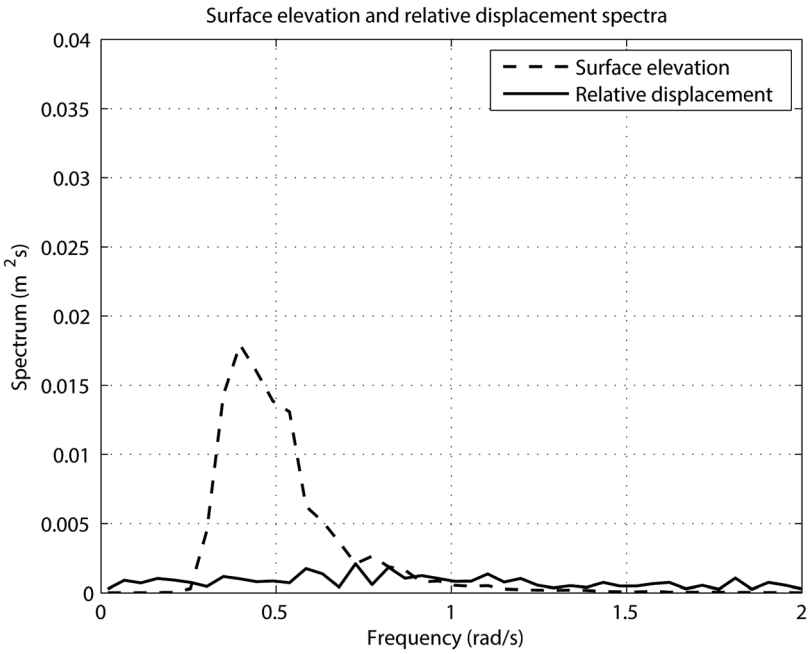

FIG. 12. Relative displacement spectrum versus surface wave spectrum.

The overdamping with $C_{DD} = 2000\,\mathrm{Ns/m}$ is easily seen in Table IV, as no power is produced because of the restricted motion. In this case, maximum power is increasing with decreasing C_{DD}. The value of $C_{DD} = 500\,\mathrm{Ns/m}$ produces the greatest magnitude peaks and the largest RMS. It seems that an optimum C_{DD} for the double-body case is $500\,\mathrm{Ns/m}$.

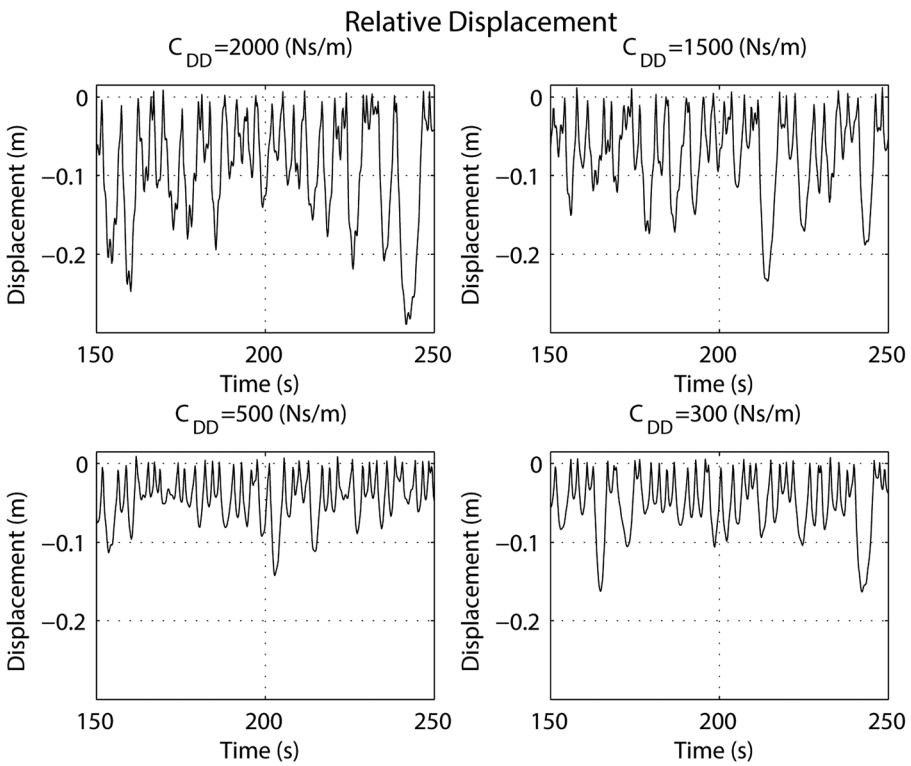

FIG. 13. Time series of the relative displacement between Body A and Body B for various C_{DD} values.

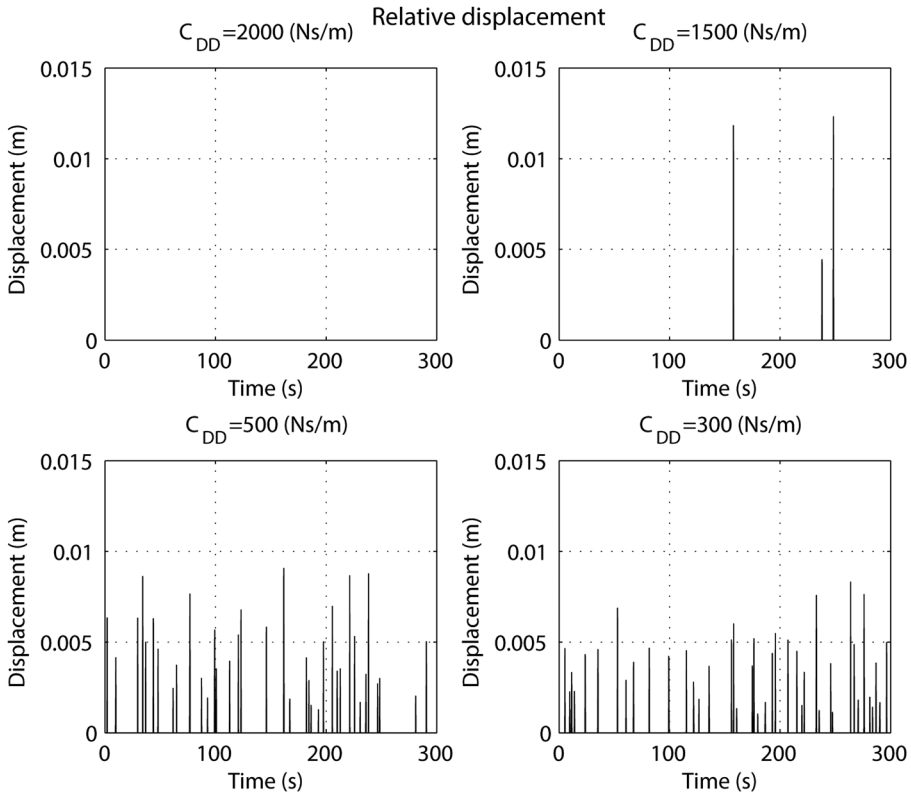

FIG. 14. The positive relative displacement between Body A and Body B that contributes to power generation for various C_{DD} values.

Furthermore, when the ballast weight of Body B was increased, there was a noticeable improvement in the RMS of power. However, caution should be taken not to add too much weight to the drogue. The numerical model cannot determine if a drogue would collapse from adding too much ballast weight.

2. Different drogue size and operational depth

A second drogue case was also considered numerically to determine if it could produce more consistent and higher power. The dimensions of this drogue are governed by the conclusions of Montgomery and Stroup.[17] The downstream spill hole should be 5% of the inlet hole (for the best stability in lateral oscillations), and a height to major diameter ratio of 2 for vertical oscillation stability. The new drogue is thus chosen such that it has 2 m height, 1.0 m diameter large spill hole, and 0.05 m small spill hole. Holler's[16] and Vachon's[14] towing-tank testing and graph of the relation between C_D and H/D are used to find the drag coefficient of 1.5 $(H/D = 1.7)$ for the experimental drogue, and a drag coefficient of 1.6 $(H/D = 2)$ is used for the numerical drogue.

Also, the two drogues were analyzed numerically for two different operational depth and water depth combinations, and the results are shown in Table V (the drogue used in the experiments of

TABLE IV. Comparison between different C_{DD} values for the double body case.

C_{DD} Cases	2000 Ns/m	1500 Ns/m	500 Ns/m	300 Ns/m
Average of power peaks	0 W	0.24 W	3.73 W	3.27 W
Maximum peak power	0 W	0.04 W	13.52 W	16.63 W
Power RMS	0 W	0.01 W	0.82 W	0.77 W

TABLE V. Numerically obtained values for different drogues.

Drogue cases	Smaller drogue 10.6 m	Larger drogue 10.6 m	Smaller drogue 100 m	Larger drogue 100 m
Average of power peaks	4.04 W	13.14 W	5.26 W	5.15 W
Maximum peak power	14.0 W	141.3 W	21.8 W	23.1 W
Power RMS	0.65 W	3.78 W	0.94 W	1.05 W

Nolte *et al.*[18] is labeled as "Smaller Drogue" and it operates at a depth (from the SWL to the top of the drogue) of 10.6 m, in water depth of about 18 m, or operates at a depth of 100 m, in water depth of 5000 m, and the drogue labeled as "Larger Drogue" is the new drogue, whose particulars are given above, operates at similar depths). As expected, the larger drogue had a greater RMS. However, when deeply submerged and in deep water, there is very little difference between the two drogues. In other words, it makes no difference to use a large drogue if the drogue is deeply submerged. This is one of the important conclusions of this study.

VI. CONCLUSIONS

When we compare the experimental data of Nolte *et al.*[18] for the single-body case with the numerical predictions obtained here, we see similar time series for the motions. The major difference is the clipping observed in the experimental data of Nolte *et al.*[18] The clipping is caused by a slight delay in the spring retracting, which causes the WEC system to delay a few seconds. This "clipping" could cause much of the difference between the numerical and experimental power results shown in Table I. The numerical model only considers a perfect system with no delay in the system.

For the double-body case, the relative vertical displacement amplitude and average peak power correspond to experimental data. However, a greater RMS and maximum amplitude of power is seen in the numerical data. This could be caused by the "clipping" or because of the assumption that the drogue always stayed directly under the WEC system; in reality, it can certainly drift differently from the WEC device, and therefore, may not be under it at all times.

Even with these differences, the numerical model provides a good comparison with the experimental data. Therefore, the present approach can be used to optimize C_{DD}, ballast weight, and $\alpha F_{constant}$ for the wave climates of any future testing. In the double-body case, the multiple drogue designs showed that a larger drogue is more stable and has a larger RMS at a shallower depth. However, if the drogue is deeply submerged, either drogue can be used as the power RMS and peak amplitudes are similar.

Comparing the spectra of the two cases, the single-body case is able to capture more of the available energy from the surface waves. The sea floor provides a stable anchor point (for the single-body case) that allows for large relative displacements. The experimental drogue does not provide a stable relative anchor point for the WEC system unless a larger-size drogue is used. It appears that a limiting factor in the double-body case is the ability of the drogue to have limited response to the PTO force and wave exciting forces. In summary, the system could be optimized for stable drogue conditions.

Finally, some control theory can be used to make the heave velocity in the single-body case synchronous with the irregular exciting force.[25] In the two-body case, the relative velocity between Body A and Body B should be synchronous with a linear combination of the exciting forces on the two bodies (which also involves the impedances of the two bodies (Ref. 26)). However, this would only be possible by having a second generator that will allow the system to produce power throughout the entire wave cycle.

ACKNOWLEDGMENTS

We gratefully acknowledge the funding of this project by the Office of Naval Research through Trex Enterprises of Maui. We thank the Program Director at ONR, Dr. Ron Joslin, and Dr. Ned

Davis who developed the WEC device at Trex Enterprises, Maui, and Dr. Murthy Chitrapu who kindly helped on various technical issues during this study. The comments of Professor Umesh Korde and the three anonymous reviewers are very much appreciated as they improved this work.

[1]Y. Washio, see http://www.takesteps.org, for wave energy research and development at JAMSTEC, September 2012 (1998).
[2]NASA, see oceanmotion.org/html/gatheringdata/buoysanddrifers.htm, for Ocean motion and surface currents. Drifters and buoys December 2012 (2013).
[3]D. Symonds, E. P. Davis, and R. C. Ertekin, "Low-power autonomous wave energy capture device for remote sensing and communications applications," in *Proceeding of IEEE Energy Conversion Congress and Exposition*, 2010, pp. 2392–2396.
[4]E. P. Davis, R. C. Ertekin, and H. R. Riggs, "A buoy-based WEC device to provide low power to sensors," in *Proceeding of 28th International Conference on Ocean, Offshore and Arctic Engineering* (OMAE, ASME, 2009), Paper No. OMAE2009-80091.
[5]S. J. Beatty, P. Wild, and B. J. Buckham, "Integration of a wave energy converter into the electricity supply of a remote Alaskan island," Renewable Energy **35**, 1203–1213 (2010).
[6]B. M. Count and E. R. Jefferys, "Wave power the primary interface," in *Proceeding of 13th Symposium on Naval Hydrodynamics, Tokyo, The Shipbuilding Research Association of Japan,* 1981, pp. 817–828.
[7]A. F. Falcão, "Phase control through load control of oscillating-body wave energy converters with hydraulic PTO system," Ocean Eng. **35**, 358–366 (2008).
[8]P. C. Vicente, A. F. Falcão, and P. Justino, "Nonlinear dynamics of a tightly moored point-absorber wave energy converter," Ocean Eng. **59**, 20–36 (2013).
[9]R. Guanche, V. Gómez, C. Vidal, and I. Eguinoa, "Numerical analysis and performance optimization of a submerged wave energy point absorber," Ocean Eng. **59**, 214–230 (2013).
[10]W. E. Cummins, "The impulse response function and ship motions," Technical Report No. 1661, David Taylor Model Basin, Hydromechanics Laboratory, R&D Report, Maryland, 1962.
[11]T. F. Ogilvie, "Recent progress toward the understanding and prediction of ship motions," in *Proceeding of 5th Symposium on Naval Hydrodynamics, Bergen, Norway*, 1964, pp. 3–80.
[12]U. A. Korde and R. C. Ertekin, "An active-controlled submerged wave energy device with energy focusing," in *Proceeding of International Conference on Ocean Energy, ICOE'2012, Dublin, Ireland, 17–19 October*, 2012.
[13]U. A. Korde and R. C. Ertekin, "On wave energy focusing and conversion in open water," Renewable Energy Int. J. **62**, 84–99 (2014).
[14]W. A. Vachon, "Scale model testing of drogues for free drifting buoys," Technical Report No. R-769, The Charles Stark Draper Laboratory, Inc., Cambridge, Massachusetts, 1973.
[15]W. A. Vachon, "Current measurement by Lagrangian drifting buoys-problems and potential," in *Proceeding of Oceans'77* (MTS-IEEE, 1977), pp. 46B1–46B7.
[16]R. A. Holler, "Hydrodynamic drag of drogues and sea anchors for drift control of free-floating buoys," in *Proceeding of Oceans'85—Ocean Engineering and the Environment* (IEEE, 1985), pp. 1330–1335.
[17]R. B. Montgomery and E. Stroup, *Equatorial Waters and Currents at 150 W in July–August 1952* (Johns Hopkins Press, Baltimore, 1962).
[18]J. Nolte, R. C. Ertekin, and E. P. Davis, "In-ocean experiments of a wave energy conversion device when moored to an anchor and to a drogue," J. Ocean Technol. **8**, 71–85 (2013).
[19]V. Keller, "Numerical model of a wave energy conversion device," Master's thesis (Department of Ocean and Resources Engineering, University of Hawaii at Manoa, 2011).
[20]HYDRAN, *A Computer Program for the Hydroelastic Response Analysis of Ocean Structures, v. 4.0.3* (OffCoast, Inc., Kailua, Hawaii, 2010).
[21]J. Nolte, "In-ocean experiments of a wave energy conversion device with a drogue and wave power calculations," Master's thesis (Department of Ocean and Resources Engineering, University of Hawaii at Manoa, 2013).
[22]J. Otto de Kat, "Large amplitude ship motions and capsizing in severe sea conditions," Ph.D. thesis (University of California, Naval Arch. and Offshore Eng., Berkeley, CA (1988).
[23]S. A. Chitrapu and R. C. Ertekin, "Time-domain simulation of large-amplitude response of floating platforms," Ocean Eng. **22**, 367–386 (1995).
[24]J. Otto de Kat, "The numerical modelling of ship motions and capsizing in severe seas," J. Ship Res. **34**, 289–301 (1990).
[25]U. A. Korde, "Up-wave surface elevation for smooth hydrodynamic control of wave energy conversion in irregular waves," in *Proceeding of Oceans 2013 Conference, MTS/IEEE, September* (2013), p. 10.
[26]J. Falnes, "Wave energy conversion through relative motion between two single–mode oscillating bodies," in Proceedings of International Conference on Offshore Mechanics and Arctic Engineering, OMAE, Lisbon, 5–9 July 1998.